AAS 20-493

# APPLICATIONS AND LIMITATIONS OF ANGLES-ONLY RELATIVE NAVIGATION USING POLYNOMIAL SOLUTIONS

**Matthew Willis*** **and Simone D'Amico†**

Initial relative orbit determination from bearing angle measurements represents an enabling technology for autonomous space missions. This work addresses the range ambiguity issue by capturing nonlinear separation effects with a second-order Cartesian relative motion model for eccentric orbits. The system of polynomial constraint equations resulting from a series of line-of-sight measurements is solved numerically by homotopy continuation. Proof-of-concept is demonstrated for a variety of orbit scenarios, including the first application of angles-only relative navigation to hyperbolic flyby trajectories. Inherent limitations of the approach resulting from sensitivity to perturbing forces, measurement error, and uncertainty in the observer state are assessed.

## INTRODUCTION

In order to sustainably grow the population of satellites in orbit and achieve increasingly ambitious exploration objectives, future space missions must rely less on ground support and more on autonomous navigation systems. The problem of initial relative orbit determination (IROD) is of particular interest for space situational awareness, on-orbit rendezvous and servicing, and orbital debris mitigation applications. It entails the estimation of a space resident object's state with respect to another spacecraft from a set of measurements, without cooperation or prior knowledge. While many sensor and measurement combinations could be applied to this problem, bearing-angle measurements from a single camera are an especially attractive option due to the ubiquity, passivity, modest price, and small form factor of these sensors. One of the challenges of angles-only relative navigation is the weak observability of the state, a problem first elaborated by Woffinden.[1] Linear dynamics models based on relative position and velocity, such as Clohessy-Wiltshire (CW) or Yamanaka-Ankersen (YA), lead to ambiguity in the range between the observer spacecraft and the target.[2,3] The relative state can only be resolved to within an unknown scale factor because any range value would produce the same set of bearing-angle measurements from the linear system. This paper explores the use of a second-order dynamics model to capture the nonlinear range behavior, with consideration for the effects of observer orbit eccentricity, unmodeled perturbations, and error in the bearing angle measurements.

Several strategies for circumventing the range ambiguity have been proposed in the literature. One is to maneuver the observer to effectively obtain stereoscopic information, offset in time.[4] This approach is undesirable due to the consumption of precious fuel and the logistical complexity of maneuver planning. Another approach is to offset the camera from the observer spacecraft's center

*PhD Candidate, Department of Mechanical Engineering, Stanford University, 496 Lomita Mall, Stanford, CA 94305.
†Professor, Department of Aeronautics and Astronautics, Stanford University, 496 Lomita Mall, Stanford, CA 94305.

of mass and use attitude maneuvers to acquire stereoscopic information.[5] While this can avoid the problem of fuel consumption, achieving the large baseline needed for range resolution requires an increase in the structural mass of the spacecraft and attitude maneuvers bring their own logistical difficulties. More favorable strategies seek to capture the range information in the dynamics model. This can be accomplished by changing the coordinate system or state representation. Woffinden's dilemma applies specifically to linear models in Cartesian coordinates, but it has been shown that the relative state is observable for linear models in curvilinear coordinates.[6] One may also change the state representation from relative position and velocity to relative orbital elements, allowing for more accurate modeling of separation-dependent Keplerian motion as well as perturbations from Earth oblateness, atmospheric drag, and so on.[7,8] This method has drawbacks for IROD due to the dependence on batch least-squares initialization using measurements spanning more than a full orbit.[9] An alternative strategy is to extend the relative position and velocity model to higher order and use the nonlinear effects to resolve the range ambiguity.[10] Although solving the nonlinear system is computationally challenging, this approach can potentially give a coarse initialization from a small number of measurements taken over a fraction of an orbit.

Various methods for solving systems of polynomial equations are provided by the branch of mathematics known as algebraic geometry. Unlike the more familiar field of linear algebra, analytical solutions to polynomial systems are only available at lower degrees and in special cases. The Abel-Ruffini theorem states that there is no general solution in radicals for polynomials of degree five or greater.[11] As a result, solutions to higher-order systems typically rely on numerical methods. Newman et al. discuss several such strategies in the context of IROD, ultimately adopting one based on Macaulay resultant theory.[12] The present work builds on that of Lovell et al., using the technique of homotopy continuation to solve the IROD measurement equations.[13] In particular, it leverages the robust tools available in the Bertini software package to efficiently solve polynomial systems.[14] This paper distinguishes itself from earlier work on the topic by considering more advanced dynamics models and, consequently, more diverse orbit regimes than previous studies.

Higher-order solutions for spacecraft relative motion have been studied since the introduction by London of the approximate second-order solution for near-circular orbits.[15] Having been independently derived multiple times, this second-order solution is commonly referred to as the Quadratic Volterra (QV) model.[16–18] Past IROD studies using polynomial models have primarily focused on the QV solution, but recent interest in the application of higher-order models to angles-only navigation has prompted the development of more accurate models. Melton used an approximation technique similar to that of London to incorporate the effect of small eccentricities into a closed-form solution.[19] This technique has been refined and extended by Butcher and others to develop families of second- and third-order solutions incorporating small eccentricity effects as well as the leading-order effect of Earth oblateness.[20,21] All of these models are explicit in time, but are based on the same near-circular-orbit assumption as CW and are therefore limited in their applicability. Willis, Lovell, and D'Amico (WLD) circumvented this limitation by extending the YA model into a second-order solution that is applicable to arbitrarily eccentric orbits.[22]

The next section introduces the polynomial measurement equations for IROD based on the WLD model and describes the method used to solve them. It includes a discussion of how to disambiguate the multiple solutions to the polynomial system. This is followed by a proof-of-concept validation based on a Keplerian truth model and ideal measurements. Parameter sweeps and Monte Carlo analysis are used to evaluate the approach's performance across a wide range of orbit eccentricities, measurement intervals, and relative states. In addition to highly elliptical orbits which would be in-

tractable for earlier polynomial dynamics models, the validation section considers hyperbolic flyby trajectories. This represents an important contribution to the state of the art by extending the utility of this field of research beyond Earth orbit. In reality, orbits are not perfectly Keplerian and it is impossible to obtain exact knowledge of the line-of-sight vector or observer state. The remainder of the paper addresses these complexities and their impact on the IROD algorithm. To understand the impact each of these assumptions has on the accuracy of the estimated state, separate validation experiments are provided for the cases of full-force orbit propagation and error in the bearing-angle measurements. Finally, the paper concludes with a review of the most important findings and outlook on future research paths.

## IROD METHODOLOGY

### Homotopy Continuation

For the angles-only IROD problem being considered, the measurements are pairs of bearing angles in the frame of a monocular camera on the observer spacecraft, taken at known points in time. With knowledge of the observer's configuration and attitude, these can be transformed from the camera frame to unit direction vectors in the observer spacecraft's body frame and ultimately its radial-transverse-normal (RTN) frame. The latter is characterized by basis vectors $\hat{\mathbf{x}}$, $\hat{\mathbf{y}}$, and $\hat{\mathbf{z}}$, where $\hat{\mathbf{x}}$ points radially away from the central body, $\hat{\mathbf{z}}$ is aligned with the observer's orbital angular momentum vector, and $\hat{\mathbf{y}} = \hat{\mathbf{z}} \times \hat{\mathbf{x}}$ completes the right-handed triad. These straightforward transformations are not considered by the present work, except for their contribution to measurement uncertainty. Similarly, the nontrivial problem of target identification and tracking is addressed elsewhere in the literature and neglected here.[23,24] Thus, the inputs to the IROD algorithm being studied are line-of-sight unit vectors expressed in the RTN frame of the observer spacecraft,

$$\hat{\mathbf{l}} = \begin{bmatrix} \ell_x \\ \ell_y \\ \ell_z \end{bmatrix} \tag{1}$$

The line-of-sight vector must be parallel with the relative position vector $\boldsymbol{\delta}\mathbf{r} = [x, y, z]^T$, so a set of constraint equations can be formed from their null cross product,

$$\hat{\mathbf{l}} \times \boldsymbol{\delta}\mathbf{r} = \begin{bmatrix} \ell_z y - \ell_y z \\ \ell_x z - \ell_z x \\ \ell_y x - \ell_x y \end{bmatrix} = \begin{bmatrix} 0 \\ 0 \\ 0 \end{bmatrix} \tag{2}$$

Any pair of these equations can be subtracted to obtain the third, so each observation provides two linearly independent equations relating the measured line-of-sight vector components to the unknown relative position coordinates at that time. The position coordinates are related to a set of six integration constants by a relative dynamics model, so combining measurements from three observation times yields a system of six equations in the six unknown constants. A general second-order relative dynamics model can be written as

$$\boldsymbol{\delta}\mathbf{r}_l = \mathbf{b}_{l1}^T \mathbf{K} + \mathbf{K}^T B_{l2} \mathbf{K} \tag{3}$$

where $l$ indexes the $x$, $y$, or $z$ component, $\mathbf{K} = [K_1, K_2, K_3, K_4, K_5, K_6]^T$ is the vector of integration constants, and the vector $\mathbf{b}_{l1}$ and matrix $B_{l2}$ contain coefficients that depend on the observer

state and time. The subscripts 1 and 2 indicate that these coefficients define the first- and second-order contributions to the relative motion.

This paper employs the recently introduced WLD model for relative motion on eccentric orbits, which is a second-order extension of the linear YA model. Both of these models are explicitly defined in the Appendix, but the WLD model can be represented as

$$\begin{aligned}
\tilde{x}(e_o, f_0, f, \mathbf{K}) &= \sum_{i=1}^{6} b_{x1,i}(e_o, f) K_i + \sum_{j \geq i}^{6} \sum_{i=1}^{6} b_{x2,ij}(e_o, f_0, f) K_i K_j \\
\tilde{y}(e_o, f_0, f, \mathbf{K}) &= \sum_{i=1}^{6} b_{y1,i}(e_o, f) K_i + \sum_{j \geq i}^{6} \sum_{i=1}^{6} b_{y2,ij}(e_o, f_0, f) K_i K_j \\
\tilde{z}(e_o, f_0, f, \mathbf{K}) &= \sum_{i=1}^{6} b_{z1,i}(e_o, f) K_i + \sum_{j \geq i}^{6} \sum_{i=1}^{6} b_{z2,ij}(e_o, f_0, f) K_i K_j
\end{aligned} \tag{4}$$

where the $b$ coefficients are functions of the observer's orbit eccentricity $e_o$, initial true anomaly $f_0$, and true anomaly at the observation time. The WLD model describes the relative position scaled by the observer's orbit radius, $\boldsymbol{\delta}\tilde{\mathbf{r}} = \boldsymbol{\delta}\mathbf{r}/r = [\tilde{x}, \tilde{y}, \tilde{z}]^T$. Because this scaling does not affect the position vector's direction, the normalized coordinates can be used directly in the formulation of the measurement equations. By construction, the $b_{(\cdot)1}$ coefficients of the linear part are identical to the YA model, while $b_{(\cdot)2}(e_o, f_0, f_0) = 0$ for the quadratic part. Letting $f_0$ correspond to the first observation, the system of measurement equations is given by

$$\begin{aligned}
\ell_{x,0}\tilde{z}(e_o, f_0, f_0, \mathbf{K}) - \ell_{z,0}\tilde{x}(e_o, f_0, f_0, \mathbf{K}) &= 0 \\
\ell_{y,0}\tilde{x}(e_o, f_0, f_0, \mathbf{K}) - \ell_{x,0}\tilde{y}(e_o, f_0, f_0, \mathbf{K}) &= 0 \\
\ell_{x,1}\tilde{z}(e_o, f_0, f_1, \mathbf{K}) - \ell_{z,1}\tilde{x}(e_o, f_0, f_1, \mathbf{K}) &= 0 \\
\ell_{y,1}\tilde{x}(e_o, f_0, f_1, \mathbf{K}) - \ell_{x,1}\tilde{y}(e_o, f_0, f_1, \mathbf{K}) &= 0 \\
\ell_{x,2}\tilde{z}(e_o, f_0, f_2, \mathbf{K}) - \ell_{z,2}\tilde{x}(e_o, f_0, f_2, \mathbf{K}) &= 0 \\
\ell_{y,2}\tilde{x}(e_o, f_0, f_2, \mathbf{K}) - \ell_{x,2}\tilde{y}(e_o, f_0, f_2, \mathbf{K}) &= 0
\end{aligned} \tag{5}$$

where the second and third constraints from Equation 2 were chosen for reasons of simplicity resulting from the details of the WLD model. Because $b_{(\cdot)2}(e_o, f_0, f_0) = 0$, the first two expressions on the left-hand side of Equation 5 are linear in the integration constants while the remainder contain both linear and quadratic terms. This greatly reduces the number of candidate solutions and computational cost of solving the system of equations.

Unlike linear systems, higher-order polynomial systems do not have general analytical solutions. However, the method of homotopy continuation can be used to obtain the solution to the desired system by transformation of the known solution to a simpler system. The essential ideas of this method are outlined below, and the interested reader can find further discussion in the work of Bates, et al.[14] Consider a homotopy

$$H(\mathbf{K}, s) = (1 - s) \begin{bmatrix} h_1(\mathbf{K}) \\ \vdots \\ h_6(\mathbf{K}) \end{bmatrix} + \gamma s \begin{bmatrix} q_1(\mathbf{K}) \\ \vdots \\ q_6(\mathbf{K}) \end{bmatrix} = \mathbf{0} \tag{6}$$

where the $h_i$ are the polynomial equations of our system, the $q_i$ are the polynomial equations of a starting system whose solution is known, $s$ is a path variable from 1 to 0, and $\gamma$ is a complex

constant incorporated for robustness. For reference, given the system in Equation 5 and definition of the WLD model in Equation 4, the $h_1(\mathbf{K})$ that appears in Equation 6 is

$$h_1(\mathbf{K}) = \sum_{i=1}^{6} \left(\ell_{x,0} b_{z1,i}(e_o, f_0) - \ell_{z,0} b_{x1,i}(e_o, f_0)\right) K_i \tag{7}$$

The starting system $H(\mathbf{K}, s = 1)$ has a known solution and we wish to find the vector $\mathbf{K}$ that solves the target system $H(\mathbf{K}, s = 0)$. Because the solution varies smoothly as $H$ is transformed from the starting system to the target system, the solution to the target system can be found by tracking the path of the integration constants $\mathbf{K}$. Taking the derivative of $H$ with respect to $s$ leads to the differential equation

$$\frac{\partial H}{\partial \mathbf{K}} \frac{d\mathbf{K}}{ds} + \frac{\partial H}{\partial s} = 0 \tag{8}$$

where $\partial H / \partial \mathbf{K}$ is the Jacobian matrix

$$\frac{\partial H}{\partial \mathbf{K}} = \begin{bmatrix} \frac{\partial H_1}{\partial K_1} & \cdots & \frac{\partial H_1}{\partial K_6} \\ \vdots & \ddots & \vdots \\ \frac{\partial H_6}{\partial K_1} & \cdots & \frac{\partial H_6}{\partial K_6} \end{bmatrix} \tag{9}$$

Solving the system amounts to numerically integrating the ordinary differential equation

$$\frac{d\mathbf{K}}{ds} = -\left[\frac{\partial H}{\partial \mathbf{K}}\right]^{-1} \frac{\partial H}{\partial s} \tag{10}$$

from $s = 1$ to $s = 0$. Because polynomial systems can have multiple solutions, there will be several paths to track and a set of candidate state estimates, $\{\bar{\mathbf{K}}\}$. How to select the best estimate from this set is the next topic to be addressed.

**Solution Disambiguation**

The maximum possible number of solutions to a polynomial system is given by Bézout's theorem, which states that a system of $\beta$ equations (in $\beta$ variables) of degree $\alpha$ has $\alpha^\beta$ solutions.[25] In the formulation of the IROD problem described above, there are four equations with degree $\alpha = 2$ and two equations with degree $\alpha = 1$, giving a total of $2^4 = 16$ possible solutions. By using a second-order dynamics model instead of a linear model such as YA, the infinite range ambiguity has been replaced with a finite range ambiguity corresponding to the finite set of solutions. Bézout's theorem gives the total number of both real and complex solutions to the system, and the method of homotopy continuation will identify all solutions of both types. It would be tempting to eliminate the complex solutions and consider only the real solutions for this physical problem, but that reasoning is incorrect. Even in the absence of measurement errors and perturbations, the imperfect representation of the relative dynamics will cause discrepancies between the line-of-sight vectors and the relative position vectors predicted by the polynomial model. As a result, the closest approximation to the true state admissible by Equation 5 may have imaginary components. This situation is especially likely in practice, when measurement noise and perturbing forces are present. Fortunately, complex solutions occur in conjugate pairs, so half of these potential estimates can be eliminated when only the real part is considered. Several physical and practical considerations can be used to further reduce the set of candidate solutions and disambiguate the relative state.

First, it is evident that Equation 5 has a trivial solution $\mathbf{K} = \mathbf{0}$, which places the target and observer in the same state. This may be immediately removed from the set of candidate solutions. Next, the measurement equations constrain $\hat{\mathbf{l}}$ and $\boldsymbol{\delta\tilde{\mathbf{r}}}$ to lie on the same line, but does not require them to have the same orientation. Thus, some solutions to Equation 5 may produce relative position vectors antiparallel to the line-of-sight vector. Several solutions may be eliminated by checking

$$\boldsymbol{\delta\tilde{\mathbf{r}}}(t_i, \bar{\mathbf{K}}) \cdot \hat{\mathbf{l}}(t_i) > 0 \tag{11}$$

for each measurement time $t_i$ and candidate solution $\bar{\mathbf{K}}$. Although eight parallel/antiparallel permutations of the three line-of-sight measurements are possible, few of these may correspond to admissible solutions to the constraint equations and some may correspond to multiple solutions. How much the set is reduced by this check will therefore vary from case to case.

Further elimination of candidate solutions should be handled on an application-specific basis. If the target is expected to be in a closed orbit, for example, the target's estimated relative state and observer's absolute state may be used to check that the target does not have escape velocity and that it's trajectory does not intersect the Earth's surface. Lower and upper bounds on the inter-spacecraft separation can also be imposed by sensor hardware and mission considerations and by the domain of validity of the polynomial dynamics model. Any remaining ambiguity can be resolved by repeating the IROD algorithm with new measurements and comparing results. The following sections assess the feasibility and practicality of the IROD algorithm using the WLD solution for eccentric orbits in the absence and presence of perturbations and measurement noise. To avoid clouding the results with mission-specific assumptions and arbitrary bounds, these analyses eliminate only the trivial solution and those that do not match the line-of-sight direction. The number of remaining candidate solutions is reported and the most accurate of these is used to compute the error in the output solution. This addresses the most crucial question of whether an accurate range estimate can be obtained from the IROD solution set.

## VALIDATION - IDEAL CASE

Before investigating the robustness or practicality of the polynomial IROD algorithm, it is essential to establish the feasibility of the approach. This proof-of-concept is achieved by testing its performance without perturbations or measurement errors, when the only inaccuracies are those inherent in the polynomial approximation of the relative dynamics. The methodology used to test the IROD algorithm is depicted schematically in Figure 1. A test scenario is defined by the observing spacecraft's Keplerian elements at the initial epoch, $\boldsymbol{\alpha} = [a, e, i, \Omega, \omega, M]$, the relative orbital elements of the target spacecraft with respect to the observer,

$$\boldsymbol{\delta\alpha} = \begin{bmatrix} \delta a \\ \delta\lambda \\ \delta e_x \\ \delta e_y \\ \delta i_x \\ \delta i_y \end{bmatrix} = \begin{bmatrix} \frac{a_t - a_o}{a_o} \\ (u_t - u_o) + (\Omega_t - \Omega_o)\cos i_o \\ e_t \cos\omega_t - e_o \cos\omega_o \\ e_t \sin\omega_t - e_o \sin\omega_o \\ i_t - i_o \\ (\Omega_t - \Omega_o)\sin i_o \end{bmatrix} \tag{12}$$

where $u = f + \omega$ is the argument of latitude, as well as the time interval $\Delta t$ between measurements. For simplicity, the analysis assumes that the line-of-sight measurements are equally spaced in time, but this is not required by the algorithm. The high-fidelity $S^3$ multi-satellite orbit propagator is

used to generate the absolute and relative state histories from which the measurements are synthesized.[26] These steps are initially performed under the assumptions of unperturbed motion and exact measurements, which will be relaxed in the next section.

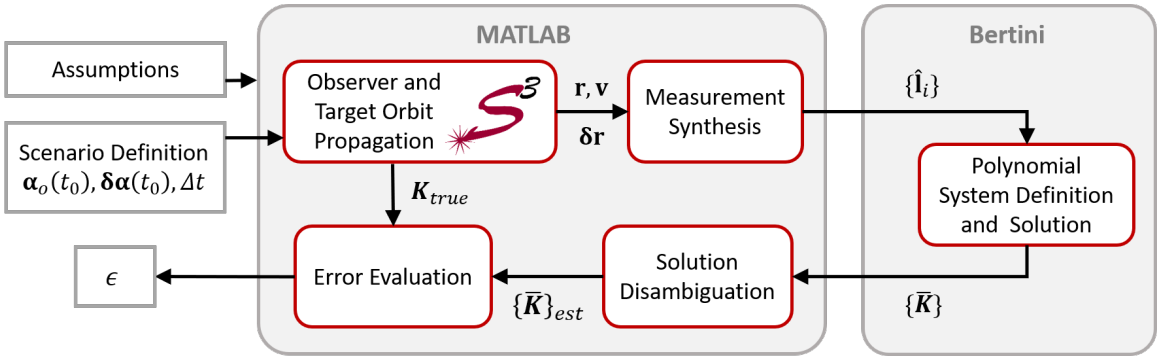


**Figure 1. Overview of validation methodology.**

Once a set of line-of-sight vectors $\{\hat{\mathbf{l}}_i\}$ has been produced, it is formulated into a polynomial system input for the Bertini software package. Bertini returns the set of solutions to the measurement equations, $\{\bar{\mathbf{K}}\}$, which are then reduced to the set of physically interesting candidate solutions $\{\bar{\mathbf{K}}\}_{est}$. Finally, the candidate solutions for the integration constants are evaluated against the true constants computed from the scenario definition. The error metric chosen for this analysis is the relative difference in estimated and true range between observer and target at the initial epoch,

$$\epsilon = \frac{\|\boldsymbol{\delta r}(t_0, \bar{\mathbf{K}}) - \boldsymbol{\delta r}(t_0, \mathbf{K}_{true})\|}{\|\boldsymbol{\delta r}(t_0, \mathbf{K}_{true})\|} \tag{13}$$

Although the full relative position and velocity state can be computed from the estimated integration constants $\bar{\mathbf{K}}$, the assessment focuses on range because the use of a polynomial dynamics model was primarily motivated by the potential to resolve the range ambiguity. With $t_0 = 0$, the relative position vector $\boldsymbol{\delta r}$ in Equation 13 is computed using the YA state transition matrix given in the Appendix.

The proof-of-concept validation is divided into two parts. First, the traditional case of an observer orbiting a central body such as the Earth is studied. Particular attention is given to the orbital eccentricity to highlight the advantages of using the WLD dynamics model in place of polynomial models for near-circular orbits considered by other authors. Next, we examine the case of an observer on a hyberbolic flyby trajectory, which has not been explored in the angles-only navigation literature.

### Elliptical Orbits

To provide a foundation for understanding the polynomial IROD approach and algorithm, we begin with an analysis of two concrete examples. Table 1 lists the observer state parameters and measurement intervals for these scenarios, which differ only in that one is near-circular and the other highly elliptical. The measurements are taken five minutes apart, shortly after perigee passage. Because the orbits are defined in terms of the perigee altitude $h_p$, the highly elliptical orbit is much larger and the measurement interval represents a smaller fraction of the orbit period. Both the dynamics model and measurement model deal with normalized parameters, so the orbit size only affects the period and there is no need to vary the altitude under the assumption of unperturbed

motion. This assumption also makes the elements $i_o$, $\Omega_o$, and $\omega_o$ irrelevant to the dynamics. They are included for their role in defining the relative orbit elements, which are the same for both scenarios and listed in Table 2. The relative motion is characterized by both in-plane and out-of-plane components, as well as a difference in semimajor axis that contributes to a drift in the along-track offset.

**Table 1. Scenario Definition for Validation Examples**

| Scenario | $h_p$ (km) | $e_o$ | $i_o$ | $\Omega_o$ | $\omega_o$ | $f_0$ | $\Delta t$ (s) |
|---|---|---|---|---|---|---|---|
| Near-Circular | 750 | 0.0001 | 98° | 30° | 30° | 20° | 300 |
| Highly Elliptical | 750 | 0.7321 | 98° | 30° | 30° | 20° | 300 |

**Table 2. Relative State Definition for Validation Examples**

| $a_o\delta a$ (km) | $a_o\delta\lambda$ (km) | $a_o\delta e_x$ (km) | $a_o\delta e_y$ (km) | $a_o\delta i_x$ (km) | $a_o\delta i_y$ (km) |
|---|---|---|---|---|---|
| 0.5 | 10 | 5 | 0 | 3 | 0 |

Figure 2 depicts the near-circular scenario in the RTN frame of the observer. The Keplerian truth model used to generate the measurements is propagated for two orbit periods from the initial epoch and the location of the target spacecraft and sightlines at the three measurement times are shown. From these vectors, the IROD algorithm produces a set of candidate solutions $\{\bar{\mathbf{K}}\}$, which are then evaluated to determine the most likely estimate of the relative state. To illuminate this process, Table 3 lists the results of the solution tests discussed in the previous section. Of the 16 solutions to the polynomial system, one is trivial and there are five complex conjugate pairs. Four of the latter and two real solutions produce relative positions antiparallel to the line-of-sight vectors at one or more measurement times. Three of the remaining solutions correspond to hyperbolic target trajectories. The last solution has a semimajor axis similar to the observer, perigee above the Earth's surface, and gives a relative error in the initial range of approximately $0.1\%$. Figure 2 includes the trajectory propagated from this estimated state according to the WLD model, illustrating both the accuracy of the model and success of the algorithm.

**Table 3. Summary of Candidate Solutions for Near-Circular Orbit Example**

| Solution | Trivial | Complex | Alignment | $a_t$ (km) | Perigee (km) | $\epsilon$ |
|---|---|---|---|---|---|---|
| 1 | Y | - | - | - | - | - |
| 2 | N | Y | N | - | - | - |
| 3 | N | Y | N | - | - | - |
| 4 | N | Y | N | - | - | - |
| 5 | N | Y | N | - | - | - |
| 6 | N | N | N | - | - | - |
| 7 | N | N | N | - | - | - |
| 8 | N | N | Y | $-8.6\times10^{-7}$ | - | - |
| 9 | N | N | Y | $-2.9\times10^{-5}$ | - | - |
| 10 | N | Y | Y | -62.7 | - | - |
| 11 | N | N | Y | 7129 | 7123 | $9.8\times10^{-4}$ |

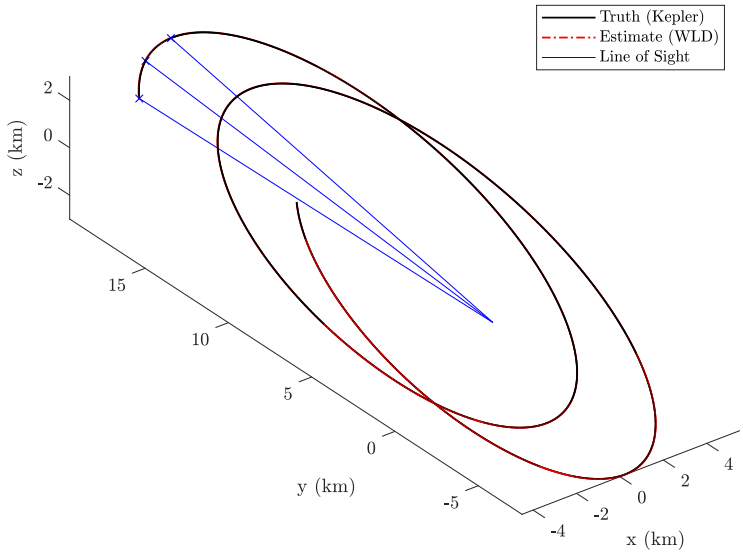


**Figure 2. Comparison of true and estimated relative motion in the observer's RTN frame for the near-circular orbit example.**

The highly elliptical orbit scenario is shown in Figure 3 and the solutions produced by the IROD algorithm are summarized in Table 4. In this case only one of the solutions gives a relative position history consistent with the line of sight measurements. That candidate solution leads to a relative error in the initial range of $0.4\%$. Although this is slightly worse than the near-circular case, it is sufficiently accurate to produce the close agreement between true and predicted motion for more than a full orbit period depicted in Figure 3 without additional measurements.

**Table 4. Summary of Candidate Solutions for Highly Elliptical Orbit Example**

| Solution | Trivial | Complex | Alignment | $a_t$ (km) | Perigee (km) | $\epsilon$ |
|---|---|---|---|---|---|---|
| 1 | Y | - | - | - | - | - |
| 2 | N | Y | N | - | - | - |
| 3 | N | Y | N | - | - | - |
| 4 | N | Y | N | - | - | - |
| 5 | N | Y | N | - | - | - |
| 6 | N | Y | N | - | - | - |
| 7 | N | Y | N | - | - | - |
| 8 | N | N | N | - | - | - |
| 9 | N | N | N | - | - | - |
| 10 | N | N | Y | 26608 | 7124 | 0.0042 |

The examples above were intended to build intuition for how the algorithm works and how readily the solution candidates can be reduced to a single relative state estimate. However, they represent isolated points in the state space. A broader sweep of the space is presented in Figure 4, showing

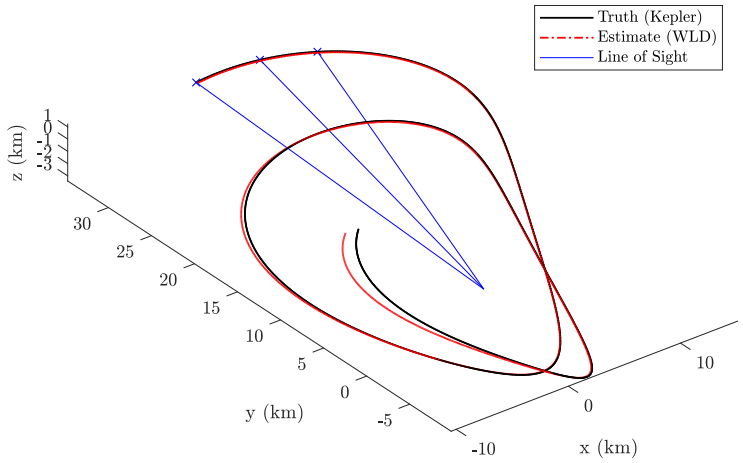


**Figure 3. Comparison of true and estimated relative motion in the observer's RTN frame for the highly elliptical example.**

the relative error in initial separation for a range of scenarios differing from the previous examples only in eccentricity, initial true anomaly, and measurement interval. To aid in readability, the curves are color-coded by initial true anomaly and style-coded by measurement interval. Using the WLD model, accuracy of the IROD estimate on the order of a few percent relative error in range is achieved for eccentricities as high as 0.95. Close to perigee (red curves in the figure) the error tends to increase with measurement interval because the polynomial model loses accuracy for longer propagations. Further from perigee (blue curves), the trend reverses and becomes more erratic for eccentric orbits due to the slower dynamics and smaller separation between measurement vectors.

Thus far only the relative state listed in Table 2 has been considered, along with a small set of observer parameters. To remove human bias from the validation process, a Monte Carlo analysis of the IROD algorithm was performed. The observer parameters from Table 1 are used, except that the eccentricity is drawn from a uniform distribution between 0 and 1 and initial true anomaly is drawn from a uniform distribution over the orbit period. The measurement interval is randomly selected as a fraction of an orbit between 0 and 0.25. Finally, each element of $a_o \boldsymbol{\delta\alpha}$ is sampled from the standard normal distribution and the entire vector is multiplied by a scale factor drawn from a logarithmically uniform distribution between $10^{2.5}$ and $10^{4.5}$ m. The initial separation between observer and target would therefore range from a few hundred meters up to a few hundred kilometers.

Figure 5 shows a histogram of the relative error in estimated range for the first measurement across 10,000 trials. On a $\log_{10}$ scale, the error distribution is roughly Gaussian, with a mean of -3.07 and standard deviation of 0.92. Thus, 88% of cases estimated the initial range to within 1% accuracy, and 98% estimated it to within 10% accuracy. Figure 6 shows plots of $\epsilon$ against orbit eccentricity, initial true anomaly, measurement interval, and maximum measurement range, including the 200-point sliding averages and 1-$\sigma$ bounds in $\log_{10} \epsilon$. The most apparent trend is a strong

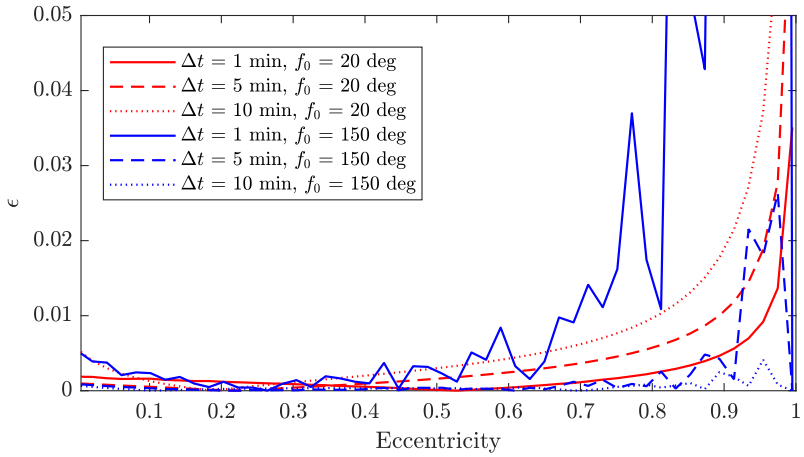


**Figure 4. Error in initial range estimate as a function of eccentricity for several scenario parameters.**

correlation between range and relative error, which follows from the second-order approximation of the relative dynamics in the polynomial model. Other noteworthy trends are more subtle in both manifestation and origin. There is a small jump in $\epsilon$ for very high eccentricities, consistent with the behavior shown in Figure 4, but there is a broader trend of decreasing $\epsilon$ as eccentricity increases. This is a consequence of uniform sampling over the orbit period, resulting in more trials close to apogee where the dynamics are slow. This also accounts for the low density of data near $f_0 = 0$ in the initial true anomaly plot. There is also a sharp uptick in $\epsilon$ for measurement intervals covering a small fraction of an orbit period.

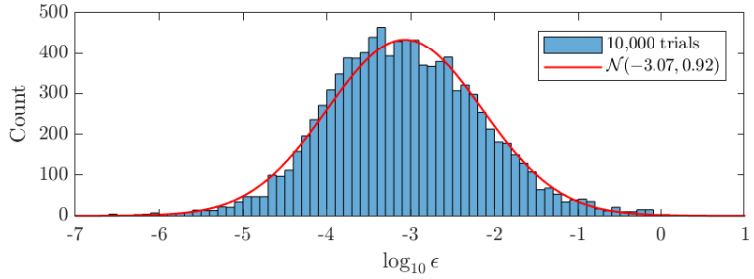


**Figure 5. Histogram of relative error results from Monte Carlo Analysis**

The Monte Carlo analysis provides further insight on the number of candidate solutions that might be produced by the algorithm and the importance of solution disambiguation. Figure 7 shows how frequently the IROD technique produced multiple unique solutions consistent with the line-of-sight directions. Nearly half of the trials led to a single candidate estimate, as was the case in the eccentric example above. About a quarter of the trials produced two candidates, and the frequency decreases steadily to a single case having nine potential estimates. Out of 10,000 trials, just twelve failed to produce any viable candidate solutions. These numbers do not reflect additional discrimination tests that could be conducted, such as orbit energy, perigee altitude, or inter-spacecraft separation. Furthermore, solutions with nontrivial imaginary components gave the most accurate estimates in nearly a third of the trials, emphasizing the need to check both real and complex solution candidates.

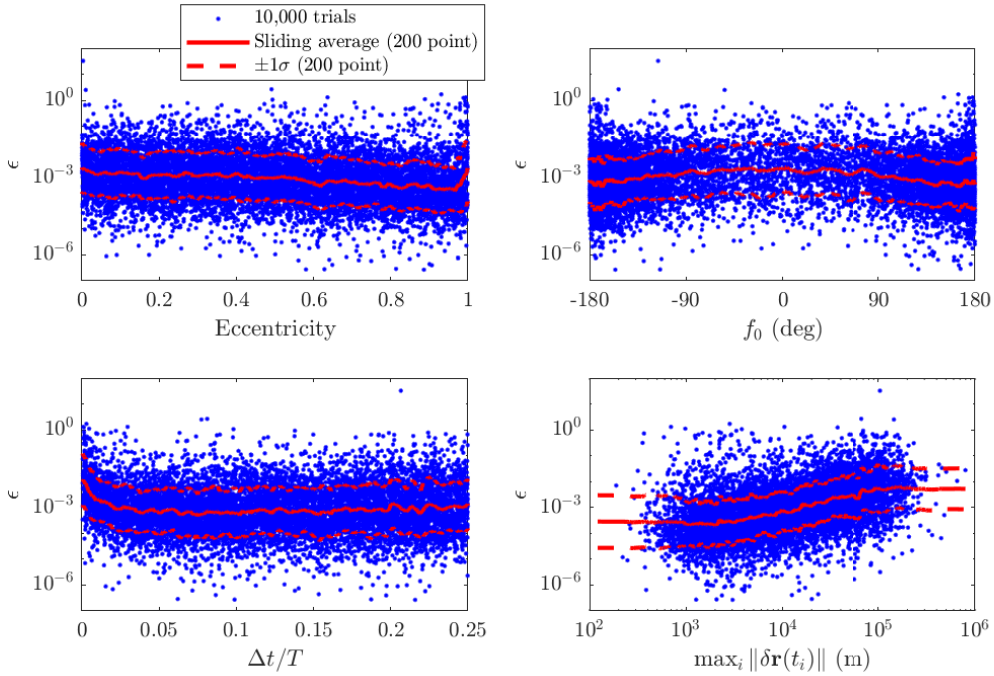


**Figure 6. Comparison of Monte Carlo error results against observer and relative state parameters.**

This need is even more important with the addition of unmodeled perturbations and measurement error, as explored in the latter part of this paper. The present analysis has demonstrated the potential for the polynomial IROD algorithm using the WLD model and a small number of measurements to estimate the range from observer to target to better than 1% accuracy across a wide range of orbit parameters. Next, we consider the case where the observer is not in orbit about the central body but performing a flyby.

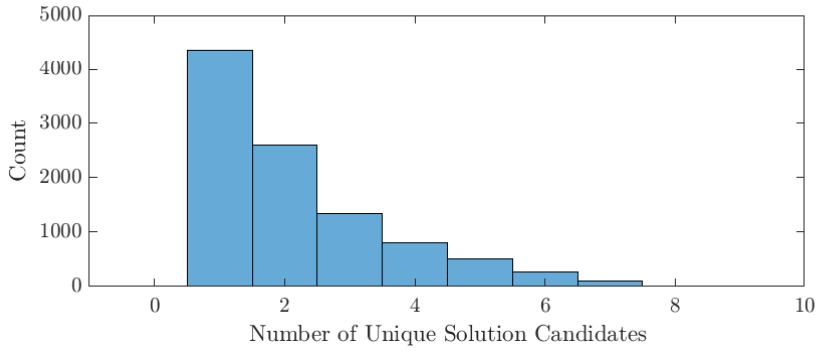


**Figure 7. Histogram of number of solution candidates from Monte Carlo Analysis**

## Hyperbolic Trajectories

Flyby trajectories have played an essential role in solar system exploration, both for gravity assistance in reaching distant targets and for the observation of celestial bodies when orbit capture is

impossible. Such trajectories have historically been reserved for monolithic spacecraft, but future exploration missions will increasingly rely on distributed architectures to increase capability and robustness at low cost. This shift has been heralded by the MarCO cubesats' Mars flyby during the entry, descent, and landing phase of the InSight mission.[27] At present, missions beyond Earth orbit rely on the Deep Space Network for both communication and navigation functions. As the population of interplanetary spacecraft grows, these missions will be subject to operational constraints imposed by the increasingly burdened communication network. Achieving this expansion while ensuring mission flexibility will only be possible with a high level of autonomy, particularly in the areas of navigation and control. The ability to determine the relative state of two spacecraft from a small number of measurements during the crucial flyby phase of an interplanetary mission is an important step in that direction. This is not possible with traditional batch orbit determination techniques that rely on many measurements over a long span of time, nor using the polynomial IROD algorithm with classical dynamics models that assume circular or near-circular orbits. However, the algorithm presented herein with the WLD model provides a unique opportunity to fill this technology gap.

In the interest of brevity, the exhaustive analysis applied to elliptical orbits is omitted in favor of a motivating example and its extension across a range of flyby eccentricities and measurement parameters. The observer parameters in Table 1 are recycled with the eccentricity raised to $e_o = 1.5$, the initial true anomaly moved to the inbound semilatus rectum, $f_0 = -90°$, and the measurement interval set to $\Delta t = 1$ min. The relative orbit elements from Table 2 are scaled up by a factor of 10 to represent a more plausible flyby scenario. The resulting true and estimated relative motion are shown in Figure 8, along with the sightlines. For this example, just one nontrivial, finite solution candidate was identified, corresponding to a relative error in the initial measurement range of $\epsilon = 5.4 \times 10^{-4}$.

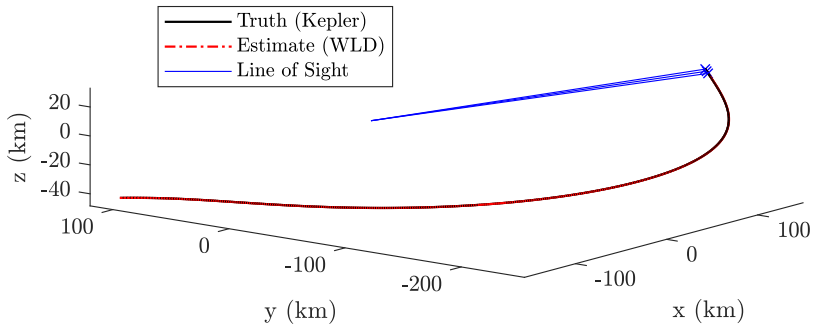


**Figure 8. Comparison of true and estimated relative motion in the observer's RTN frame for the hyperbolic flyby example with $e_o = 1.5$.**

Now that relative state determination on a hyperbolic flyby trajectory has been demonstrated for a specific example, we consider the behavior as eccentricity is varied and observations are taken at different parts of the orbit. Figure 9 shows error results for a range of scenarios closely related to the example in Figure 8. In addition to measurements taken at $f_0 = -90°$, shortly before the flyby, the figure includes the case of measurements taken at perigee. As was observed in Figure 4, poor results are obtained in the vicinity of $e_o = 1$ due to the singularity of the WLD model in this limiting case.

However, errors on the order of just a few percent result from measurements taken near perigee on more eccentric trajectories, and below 1% for measurements taken at $f_0 = -90°$. The dip to zero in $\epsilon$ near $e_o = 1.02$ is caused by the range error changing sign. The lower accuracy near perigee is a consequence of the rapid dynamics during this part of the flyby being imperfectly described by the second-order model. This preliminary analysis opens the door to a new and exciting application of angles-only IROD techniques beyond earth orbit.

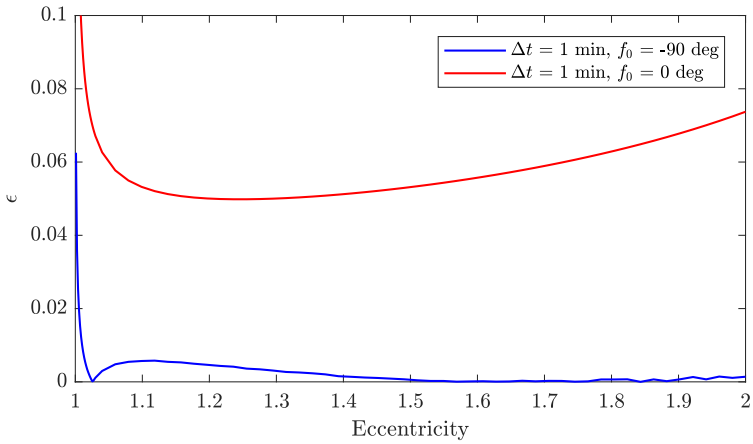


**Figure 9. Error in initial range estimate as a function of flyby eccentricity for measurements taken at $f_0 = 90°$ and at $f_0 = 0°$.**

## VALIDATION - PRACTICAL CONSIDERATIONS

### Unmodeled Dynamics

All of the analysis thus far has been performed under the assumptions of unperturbed, Keplerian motion and exact line-of-sight measurements. In reality, disturbing forces in the space environment affect the relative motion and the measurement accuracy is limited by the resolution of the optical sensor and uncertainty in the observer attitude and absolute state. Although both errors act in conjunction to corrupt the IROD problem, it is possible to address each independently with a more accurate dynamics model and higher resolution camera. It is therefore helpful in a first analysis such as this to consider their effects separately and determine to what extent each must be suppressed. The impact of unmodeled perturbations will be examined first, followed by the sensitivity to measurement errors in the next section.

Spacecraft are subject to a variety of forces not accounted for in the Keplerian model, including the nonspherical gravitational field of the central body, the gravitational attraction of third bodies such as the sun and moon, atmospheric drag, and solar radiation pressure. Since each of these depends differently on the various absolute and relative state parameters, as well as on the epoch, their presence complicates the error analysis. Different effects will have more significant contributions in different scenarios, so attempting to isolate the impact of each would be impractical at this stage. The present analysis will instead focus on how much the unmodeled dynamics degrade the accuracy in the range estimate compared to the unperturbed case. The validation procedure outlined in Figure 1 will still be used, with the assumptions modified to include a full-force propagation based on the simulation settings in Table 5 and spacecraft parameters in Table 6.

**Table 5. Full-Force Simulation Settings**

| Setting | Description |
|---|---|
| Integrator | Runge-Kutta (Dormand-Prince) |
| Time Step (s) | Fixed: $\Delta t/50$ |
| Atmospheric Drag Model | NRLMSISE00 |
| Gravity Model | GGM01S (5x5) |
| Solar Radiation Pressure | Cross-section normal to sun, no eclipses |
| Third Body Effects | Moon and Sun Point Mass, Analytical Ephemerides |

**Table 6. Spacecraft Parameters**

| Parameter | Observer | Target |
|---|---|---|
| Mass (kg) | 150 | 150 |
| $A_{drag}$ (m$^2$) | 1.3 | 1.3 |
| $A_{SRP}$ (m$^2$) | 2.5 | 2.0 |
| $C_d$ | 2.5 | 2.5 |
| $C_r$ | 1.3 | 1.3 |

In contrast to the Keplerian case, the perturbation environment depends greatly on orbit altitude and inclination, so these will be the focus of the analysis. The other observer orbital elements will match those in Table 1 for the near-circular case and the relative state will match that of Table 2. Figure 10 shows the error in the initial range estimate as a function of semimajor axis for several measurement time intervals with $i_o = 98°$. To account for the variation in orbit period $T_{orb}$ with semimajor axis, the measurement interval $\Delta t$ is defined as a fraction of an orbit period instead of a fixed time. The polar orbit results demonstrate the strong dependence on orbit altitude, but the error estimate is not acceptably accurate for any value of $a_o$ or $\Delta t$.

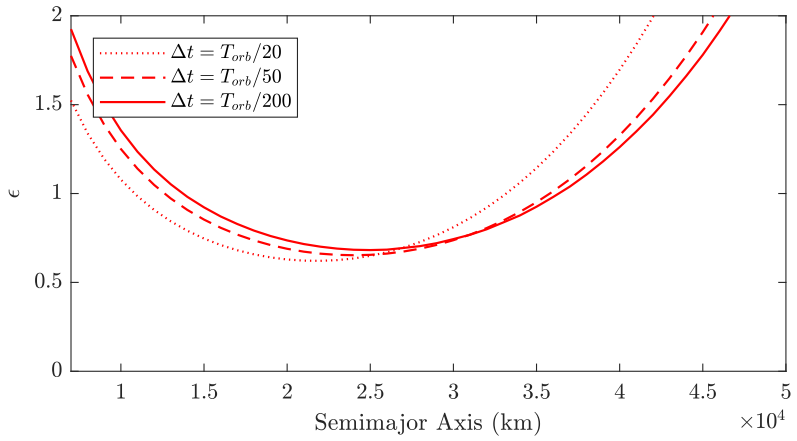


**Figure 10. Error in initial range estimate as a function of orbit semimajor axis for $i_o = 98°$.**

The situation is improved when the orbit inclination is reduced to $i_o = 30°$ and $i_o = 0°$, as shown in Figures 11 and 12, respectively. In each of these cases there is a narrow region of altitudes for

which range errors below a tolerable level of 20% for an initial estimate are obtained. The presence of this intermediate region is the result of nonspherical gravity and atmospheric drag effects growing weaker with altitude while the effects of third bodies and solar radiation pressure grow stronger, and their competing influence on the relative motion. Its location and breadth will depend on other parameters of the absolute and relative motion. A second noteworthy aspect of Figures 11 and 12 is the increase in sensitivity to perturbation effects with measurement interval. Measurements spaced more closely give more accurate estimates because the unmodeled dynamics have less time to propagate.

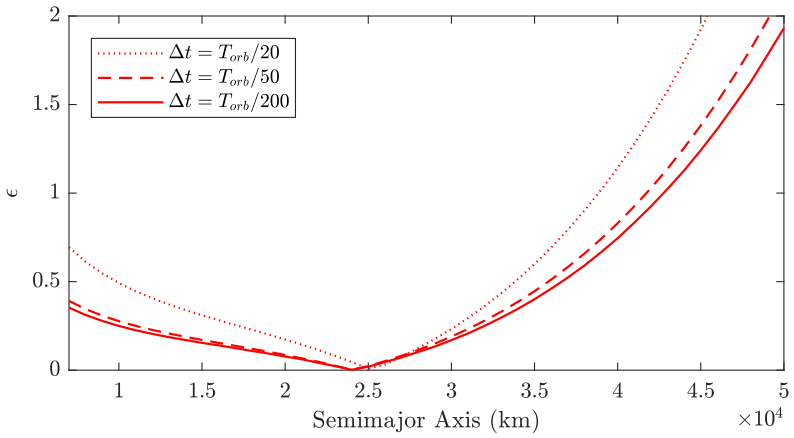


**Figure 11. Error in initial range estimate as a function of orbit semimajor axis for $i_o = 30°$.**

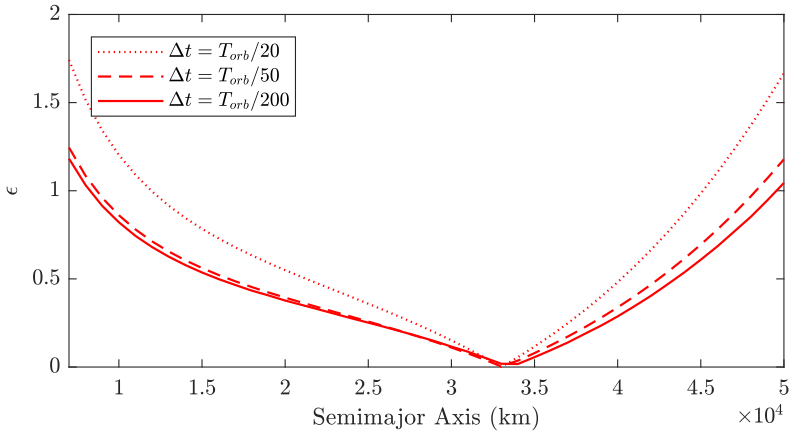


**Figure 12. Error in initial range estimate as a function of orbit semimajor axis for $i_o = 0°$.**

It is apparent from this analysis that even in the absence of measurement noise, the unmodeled forces prevent the IROD approach using WLD or the simpler QV model from producing an acceptable estimate of the relative state in all but a narrow range of scenarios. Making the approach practical will require, at a minimum, dynamics models that account for the most significant perturbations. For low-earth orbit applications these would include atmospheric drag and earth oblateness. Such additions would result in a more complicated model, but might not greatly increase the computational cost of the technique because the polynomial coefficients are only computed once at the

beginning of the algorithm. However, it will be shown in the next section that more fundamental algorithmic changes are needed to handle noise in the line-of-sight measurements.

**Measurement Error**

All of the preceding analysis has assumed perfect knowledge of the observer state as well as of the line-of-sight vector components, even in the presence of unmodeled dynamics. For a real mission, there will be uncertainty in the observer orbital parameters that appear in the WLD model, namely its semimajor axis, eccentricity, and true anomaly. There will also be errors in its attitude knowledge, which combine with the orbital state errors to corrupt the transformation of measurements from camera frame to RTN frame. Furthermore, the accuracy of the bearing angle measurements themselves is limited by the camera resolution. Each of these factors contributes to error in the line-of-sight vectors. While the sensitivity of the dynamics model to error in the observer state is important to consider, this analysis will focus on the more pernicious problem of measurement error.

Without performing any simulations, it is easy to show using back-of-the-envelope calculations that measurement uncertainty will pose a major challenge to any attempt to extract range information from the second-order relative motion dynamics. Consider a general second-order model as written in Equation 3, which computes a normalized state $x$ from the integration constants $K$. The model can be expressed as

$$x = x_1 + x_2 \tag{14}$$

where $x_1$ is linear in $K$ and $x_2$ is quadratic in $K$. That is, $x_1$ is proportional to $K$ and $x_2$ is proportional to $K^2$. The range $\delta r$ is proportional to $x$ scaled by the orbit radius $r$. The order of magnitude of the integration constants is approximated by $K \sim \delta r/r$. Using the small-angle approximation, the angular contribution $\theta_2$ of the second-order effects scales as

$$\theta_2 \sim \frac{x_2}{\delta r} \sim \frac{rK^2}{\delta r} \sim \frac{\delta r}{r} \tag{15}$$

Substituting a range of 10 km and orbit radius of 7,000 km, we would expect $\theta_2$ to be on the order of $0.1^\circ$. This represents the combined precision in bearing angle measurements, attitude knowledge, and observer state knowledge needed to resolve the second-order effects.

The detrimental effects of measurement errors will be assessed using the example scenarios defined in Tables 1 and 2. Unlike the proof-of-concept demonstrations shown in Figures 2 and 3, the line-of-sight vectors will now be computed from

$$\hat{\mathbf{l}}_{i,meas} = R_z(\theta_z)R_y(\theta_y)R_x(\theta_x)\hat{\mathbf{l}}_{i,true} \tag{16}$$

where $\theta_x$, $\theta_y$, and $\theta_z$ are small noise angles sampled from a zero-mean Gaussian distribution with standard deviation $\sigma$. Figure 13 shows the error results for the near-circular and highly elliptical scenarios for noise levels ranging from $\sigma = 10^{-4}$ to $10^2$ arcsec. The error bars show the standard deviation in $\epsilon$ across 200 trials at each noise level. For vanishingly small noise levels the relative error in the initial range matches that obtained under the ideal assumptions considered before, close to 0.1% for the near-circular case and 0.4% for the highly elliptical case. However, the sensitivity results for increasing $\sigma$ bear out the conclusions of the order-of-magnitude calculations above. The mean $\epsilon$ begins to rise steadily as the noise level increases above $\sigma = 10^{-1}$ arcsec, close to the highest pointing accuracy of 0.05 arcsec reported in the literature for a commercial star tracker.[28] Consistently obtaining better than 20% error in the initial range estimate requires measurement error

on the order of a few arcseconds or less, on the low end of typical star tracker pointing errors.[29] As the noise level approaches $10^2$ arcseconds, around the $0.1^\circ$ estimate of the preliminary analysis, no useful range information is provided by the second-order effects and the error in the estimated range is comparable to the range itself. This severely restricts the acceptable uncertainty in the observer state before the effects of perturbations are even taken into consideration.

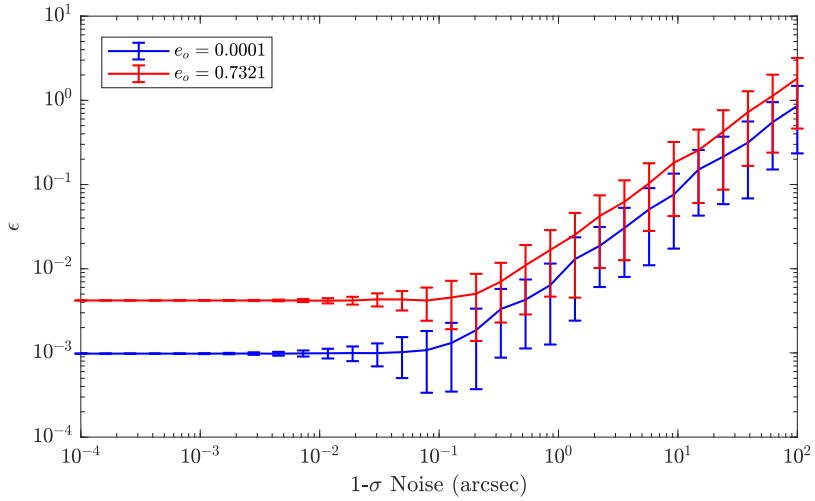


**Figure 13. Sensitivity of IROD range estimate to measurement noise.**

It may be possible to work around the method's sensitivity to measurement error and state uncertainty through several paths. First, a modified version of the algorithm which incorporates additional measurement could mitigate the problem of over-fitting to the noise. This strategy has the downside of extending the measurement period and thereby undermining the polynomial method's primary advantage over other IROD techniques. Another option would be to sample measurements from a statistical distribution around the actual measurement, producing a distribution of candidate solutions that characterizes the uncertainty and most likely contains the true state. Finally, this analysis has modeled the errors as uncorrelated in time. While this model is appropriate for noise in the bearing angle measurements in the camera frame, it does not account for bias in the observer's attitude and orbital state parameters. Such bias would have a persistent effect on the measurements that could be simultaneously estimated and removed. All of these modifications increase the computational cost and may only be practical with a highly streamlined method for solving the polynomial measurement equations.

## CONCLUSION

This paper examined the feasibility of an initial relative orbit determination algorithm based on angles-only measurements of the target spacecraft and a second-order translational state model for the relative motion on eccentric orbits. The problem boils down to solving a system of six polynomial equations in the six unknown integration constants of the dynamics model. Several techniques exist for solving such systems and the method of homotopy continuation was adopted for this analysis. Because two of the measurement equations are linear and four are quadratic, the range ambiguity is reduced from a continuum to at most sixteen candidate solutions. Methods of systematically eliminating candidates were discussed, including removal of the trivial solution, verifying

the consistency of the predicted relative motion with the observed measurement directions, checking for closed orbits, perigee altitudes above the Earth's surface, and placing plausibility bounds on the range. In practice, few candidates are physically reasonable and selecting the best estimate is simple.

Through a combination of concrete examples and Monte Carlo exploration of the parameter space, the approach was found to work well under the assumptions of unperturbed motion and precise line-of-sight measurements. Typical range errors on the order of 0.1% were observed across a wide range of orbit eccentricities, inter-spacecraft separations, and measurement intervals. Given the idealized assumptions, the residual error in the estimated state can be attributed to approximation errors in the polynomial dynamics model. This gives a lower-bound for attainable accuracy. In practice, the effects of unmodeled forces on the satellite motion and errors in the line-of-sight measurements would severely limit the accuracy and viability of the algorithm. A more accurate dynamics model is needed to address the error caused by perturbations. The need for precise measurements to resolve the second-order separation effects on the relative motion also limits the practicality of the approach. However, this could potentially be alleviated through the inclusion of additional measurements or appropriate uncertainty handling within the algorithm. Further work is also needed to develop a computationally efficient implementation that would be suitable for flight hardware and robustly resolves the solution ambiguity.

Despite its limitations, the IROD approach paired with the WLD dynamics model offers the novel application of relative state estimation on hyperbolic flyby trajectories using angles-only measurements. Due to the limited duration of hyperbolic flyby trajectories, this domain is not accessible to angles-only IROD techniques that require measurements over a full orbit. The feasibility of this use case was demonstrated through a sample scenario under idealizing assumptions. Future work should study this use case more thoroughly, applying the same noise and modeling sensitivity analyses applied herein to elliptical orbits, and considering more realistic mission scenarios. Autonomous relative navigation could reduce the dependence of interplanetary missions on the overburdened Deep Space Network, increasing flexibility and promoting exploration. This offers an exciting and previously unrecognized application beyond Earth orbit for the angles-only IROD approach using polynomial dynamics.

## ACKNOWLEDGMENTS

This work was supported by the NASA Office of the Chief Technologist's Space Technology Research Fellowship, NASA grant number 80NSSC18K1176.

## REFERENCES

[1] D. C. Woffinden and D. K. Geller, "Observability Criteria for Angles-Only Navigation," *IEEE Transactions on Aerospace and Electronic Systems*, Vol. 45, No. 3, 2009, pp. 1194–1208.

[2] W. H. Clohessy and R. S. Wiltshire, "Terminal Guidance System for Satellite Rendezvous," *Journal of Guidance, Control, and Dynamics*, Vol. 27, No. 9, 1960, pp. 653–658.

[3] K. Yamanaka and F. Ankersen, "New State Transition Matrix for Relative Motion on an Arbitrary Elliptical Orbit," *Journal of Guidance, Control, and Dynamics*, Vol. 25, No. 1, 2002, pp. 60–66.

[4] D. C. Woffinden and D. K. Geller, "Optimal Orbital Rendezvous Maneuvering for Angles-Only Navigation," *Journal of Guidance, Control, and Dynamics*, Vol. 32, No. 4, 2009, pp. 1382–1387.

[5] D. K. Geller and I. Klein, "Angles-Only Navigation State Observability During Orbital Proximity Operations," *Journal of Guidance, Control, and Dynamics*, Vol. 37, No. 6, 2014, pp. 1976–1983.

[6] D. K. Geller and T. A. Lovell, "Angles-Only Initial Relative Orbit Determination Performance Analysis using Cylindrical Coordinates," *Journal of Astronautical Sciences*, Vol. 64, 2017, pp. 72–96.

[7] J. Sullivan and S. D'Amico, "Nonlinear Kalman Filtering for Improved Angles-Only Navigation Using Relative Orbital Elements," *Journal of Guidanced, Control, and Dynamics*, Vol. 40, No. 9, 2017, pp. 2183–2200.

[8] A. W. Koenig and S. D'Amico, "Observability-Aware Numerical Algorithm for Angles-Only initial Relative Orbit Determination," AAS/AIAA Astrodynamics Specialist Conference, South Lake Tahoe, CA, August 9-13, 2020.

[9] J. Sullivan, T. A. Lovell, and S. D'Amico, "Angles-Only Navigation for Autonomous On-Orbit Space Situational Awareness Applications," AAS/AIAA Astrodynamics Specialist Conference, Snowbird, UT, August 19-23, 2018.

[10] T. Henderson, T. A. Lovell, A. Sizemore, K. Horneman, and D. Zuehlke, "Initial Relative Orbit Determination Solutions Using Polynomial Systems," 29th AAS/AIAA Space Flight Mechanics Meeting, Ka'anapali, Maui, HI, January 13-17, 2019.

[11] I. Stewart, *Galois Theory*. Chapman Hall/CRC, 3rd ed., 2004.

[12] B. Newman, T. A. Lovell, E. Pratt, and E. Duncan, "Quadratic Hexa-Dimensional Solution for Relative Orbit Determination," AAS/AIAA Astrodynamics Specialist Conference, San Diego, CA, August 4-7, 2014.

[13] T. A. Lovell, K. Horneman, A. Sizemore, and B. Morton, "Angles Only Initial Orbit Determination: Comparison of Relative Dynamics and Inertial Dynamics Approaches with Error Analysis," 28th AAS/AIAA Space Flight Mechanics Meeting, Kissimmee, FL, January 8-12, 2018.

[14] D. J. Bates, J. D. Hauenstein, A. J. Sommese, and C. W. Wampler, *Numerically Solving Polynomial Systems with Bertini*. SIAM, 2013.

[15] H. S. London, "Second Approximation to the Solution of the Rendezvous Equations," *AIAA Journal*, Vol. 1, No. 7, 1963, pp. 1691–1693.

[16] M. L. Anthony and F. T. Sasaki, "Rendezvous Problem for Nearly Circular Orbits," *AIAA Journal*, Vol. 3, No. 7, 1965, pp. 1666–1673.

[17] M. T. Stringer, B. A. Newman, T. A. Lovell, and A. Omran, "Analysis of a New Nonlinear Solution of Relative Orbital Motion," 23rd International Symposium on Space Flight Dynamics, Pasadena, California, October 29-November 2, 2012.

[18] B. A. Newman, A. J. Sinclair, T. A. Lovell, and A. Perez, "Comparison of Nonlinear Analytical Solutions for Relative Orbital Motion," AAS/AIAA Astrodynamics Specialist Conference, San Diego, California, August 4-7, 2014.

[19] R. G. Melton, "Time-Explicit Representation of Relative Motion Between Elliptical Orbits," *Journal of Guidance, Control, and Dynamics*, Vol. 23, No. 4, 2000, pp. 604–610.

[20] E. A. Butcher, E. Burnett, and T. A. Lovell, "Comparison of Relative Orbital Motion Perturbation Solutions in Cartesian and Spherical Coordinates," 27th AAS/AIAA Space Flight Mechanics Meeting, San Antonio, Texas, February 5-9, 2017.

[21] E. Burnett, E. A. Butcher, A. J. Sinclair, and T. A. Lovell, "Linearized Relative Orbital Motion Model About an Oblate Body Without Averaging," AAS/AIAA Astrodynamics Specialist Conference, Snowbird, Utah, August 19-23, 2018.

[22] M. Willis, T. A. Lovell, and S. D'Amico, "Second Order Analytical Solution for Relative Motion on Arbitrarily Eccentric Orbits," 29th AAS/AIAA Space Flight Mechanics Meeting, Ka'anapali, Maui, Hawaii, January 13-17, 2019.

[23] J. Kruger and S. D'Amico, "Autonomous Angles-Only Multi-Target Tracking for Spacecraft Swarms," AAS/AIAA Astrodynamics Specialist Conference, South Lake Tahoe, CA, August 9-13, 2020.

[24] D. Zuehlke, T. Henderson, T. A. Lovell, and A. Sizemore, "An End-to-End Process for Local Space Situational Awareness from Optical Observers," IEEE/ION Position, Location and Navigation Symposium (PLANS), Portland, OR, April 20-23, 2020.

[25] A. McLennan, "The Expected Number of Real Roots of a Multihomogeneous System of Polynomial Equations," *American Journal of Mathematics*, Vol. 124, No. 1, 2002, pp. 49–73.

[26] V. Giralo and S. D'Amico, "Development of the Stanford GNSS Navigation Testbed for Distributed Space Systems," Institute of Navigation, International Technical Meeting, Reston, VA, January 29 - February 1, 2018.

[27] A. Klesh, B. Clement, C. Colley, *et al.*, "MarCO: Early Operations of the First CubeSats to Mars," 32nd AIAA/USU Small Satellite Conference, SSC18-WKIX-04, Logan, UT, August 4-9, 2018.

[28] D. Michaels and J. Speed, "Ball Aerospace Star Tracker Achieves High Tracking Accuracy for a Moving Star Field," IEEE Aerospace Conference, Big Sky, MT, March 5-12, 2005.

[29] C. C. Liebe, "Star Trackers for Attitude Determination," *IEEE Aerospace and Electronic Systems Magazine*, Vol. 10, No. 6, 1995, pp. 10–16.

## APPENDIX: RELATIVE DYNAMICS MODELS FOR ECCENTRIC ORBITS

The first- and second-order Cartesian solutions for relative motion on eccentric orbits are presented below. Both are based on transformed versions of the position and velocity vectors of the target relative to the observer with respect to the latter's RTN frame. The coordinates are normalized by the observer's orbit radius $r$ and true anomaly $f$ replaces time as the independent variable according to

$$\begin{aligned} \boldsymbol{\delta}\tilde{\mathbf{r}} &= \frac{1}{r}\boldsymbol{\delta}\mathbf{r} \\ \boldsymbol{\delta}\tilde{\mathbf{v}} &= -\frac{e}{p}\boldsymbol{\delta}\mathbf{r}\sin f + \frac{1}{k^2\rho p}\boldsymbol{\delta}\mathbf{v} \end{aligned} \tag{17}$$

where the parameters $k^2$ and $p$ are given by

$$k^2 = \sqrt{\frac{\mu}{p^3}} \tag{18}$$

$$\rho = \frac{p}{r} = 1 + e\cos f \tag{19}$$

The inverse transformations used to restore the relative position and velocity are

$$\begin{aligned} \boldsymbol{\delta}\mathbf{r} &= r\boldsymbol{\delta}\tilde{\mathbf{r}} \\ \boldsymbol{\delta}\mathbf{v} &= k^2 p\left(e\boldsymbol{\delta}\tilde{\mathbf{r}}\sin f + \rho\boldsymbol{\delta}\tilde{\mathbf{v}}\right) \end{aligned} \tag{20}$$

Substituting the above transformations into the equations of relative motion and linearizing leads to a system of equations for $\tilde{x}$, $\tilde{y}$, and $\tilde{z}$, the transformed radial, transverse, and normal coordinates, respectively. The Yamanaka-Ankersen (YA) model solves this linear system in terms of the integral

$$J = \int_{f_0}^{f} \frac{d\tau}{\rho(\tau)^2} = k^2(t - t_0) \tag{21}$$

Written in terms of integration constants $K_1$ through $K_6$, the YA model is given by

$$\begin{bmatrix} \tilde{x} \\ \tilde{y} \\ \tilde{z} \\ \tilde{x}' \\ \tilde{y}' \\ \tilde{z}' \end{bmatrix} = \begin{bmatrix} \left(1 - \frac{3}{2}e\rho J\sin f\right) & \rho\sin f & \rho\cos f & 0 & 0 & 0 \\ -\frac{3}{2}\rho^2 J & (1+\rho)\cos f & -(1+\rho)\sin f & 1 & 0 & 0 \\ 0 & 0 & 0 & 0 & \sin f & \cos f \\ -\frac{3}{2}e\left((\rho\sin f)'J + \frac{\sin f}{\rho}\right) & (\rho\sin f)' & (\rho\cos f)' & 0 & 0 & 0 \\ \frac{3}{2}(2e\rho J\sin f - 1) & -2\rho\sin f & e - 2\rho\cos f & 0 & 0 & 0 \\ 0 & 0 & 0 & 0 & \cos f & -\sin f \end{bmatrix} \begin{bmatrix} K_1 \\ K_2 \\ K_3 \\ K_4 \\ K_5 \\ K_6 \end{bmatrix} \tag{22}$$

where $(\rho\sin f)' = \cos f + e\cos 2f$ and $(\rho\cos f)' = -(\sin f + e\sin 2f)$. To express the solution in terms of initial conditions, one may solve for the integration constants by inverting Equation (22)

and evaluating at the initial time $t_0$. Using $J(t_0) = 0$, this leads to

$$\begin{bmatrix} K_1 \\ K_2 \\ K_3 \\ K_4 \\ K_5 \\ K_6 \end{bmatrix} = \begin{bmatrix} \frac{6\rho_0+2e^2-2}{1-e^2} & 0 & 0 & \frac{2e\rho_0 \sin f_0}{1-e^2} & \frac{2\rho_0^2}{1-e^2} & 0 \\ -3\left(1+\frac{e^2}{\rho_0}\right)\frac{\sin f_0}{1-e^2} & 0 & 0 & \frac{\rho_0 \cos f_0 - 2e}{1-e^2} & -\frac{1+\rho_0}{1-e^2}\sin f_0 & 0 \\ -3\frac{e+\cos f_0}{1-e^2} & 0 & 0 & -\frac{\rho_0 \sin f_0}{1-e^2} & -\frac{e+(1+\rho_0)\cos f_0}{1-e^2} & 0 \\ -3e\left(1+\frac{1}{\rho_0}\right)\frac{\sin f_0}{1-e^2} & 1 & 0 & \frac{e\rho_0 \cos f_0 - 2}{1-e^2} & -e\frac{1+\rho_0}{1-e^2}\sin f_0 & 0 \\ 0 & 0 & \sin f_0 & 0 & 0 & \cos f_0 \\ 0 & 0 & \cos f_0 & 0 & 0 & -\sin f_0 \end{bmatrix} \begin{bmatrix} \tilde{x} \\ \tilde{y} \\ \tilde{z} \\ \tilde{x}' \\ \tilde{y}' \\ \tilde{z}' \end{bmatrix}_0 \tag{23}$$

The combination of Equations 22 and 23 is the YA state transition matrix.

The Willis-Lovell-D'Amico (WLD) model is a second-order extension of YA, constructed so that the higher-order terms vanish at $t = 0$. It's position components are given by

$$\begin{aligned}
\tilde{x} &= K_1\left(1 - \frac{3}{2}e\rho J \sin f\right) + K_2\rho \sin f + K_3\rho \cos f \\
&\quad + c_{xj}\left(1 - \frac{3}{2}e\rho J \sin f\right) + c_{xs}\rho \sin f + c_{xc}\rho \cos f - K_2K_4 \cos f + K_3K_4 \sin f \\
&\quad + \frac{1}{4}\left(K_1^2 - (K_2^2 + K_3^2)(1+\rho) - 2K_4^2 - K_5^2 - K_6^2\right) \\
&\quad - \frac{9}{8}K_1^2\rho^3J^2 + \frac{3}{2}(K_1K_2 \cos f - K_1K_3 \sin f + K_1K_4)\rho^2J - K_5K_6\frac{2e \sin f + \sin 2f}{2(1-e^2)} \\
&\quad + \frac{1}{4}\left((1+\rho)(K_3^2 - K_2^2) + K_5^2 - K_6^2\right)\cos 2f + K_2K_3\frac{(1+\rho)}{2}\sin 2f \\
\tilde{y} &= K_4 + K_2(1+\rho)\cos f - K_3(1+\rho)\sin f - \frac{3}{2}K_1\rho^2J \\
&\quad + c_{xs}\left((1+\rho)\cos f - (1+\rho_0)\cos f_0\right) - c_{xc}\left((1+\rho)\sin f - (1+\rho_0)\sin f_0\right) - \frac{3}{2}c_{xj}\rho^2J \\
&\quad + \frac{3}{2}K_1K_2\rho J \sin f + \frac{3}{2}K_1K_3(e + \cos f)\rho J - \frac{3}{2}K_1K_4e\rho J \sin f \\
&\quad + (K_3^2e - K_2K_4)(\sin f - \sin f_0) - \left(K_2K_3e + K_3K_4 + K_5K_6\frac{2e}{1-e^2}\right)(\cos f - \cos f_0) \\
&\quad - \frac{1}{2}\left(K_2K_3 + \frac{K_5K_6}{1-e^2}\right)(\cos 2f - \cos 2f_0) + \frac{1}{4}(K_3^2 - K_2^2 + K_6^2 - K_5^2)(\sin 2f - \sin 2f_0) \\
\tilde{z} &= K_5 \sin f + K_6 \cos f \\
&\quad + \left((K_3K_6 - K_2K_5)\sin^3 f_0 - 3K_3K_6 \sin f_0 + (K_2K_6 + K_3K_5)\cos^3 f_0\right)\sin f \\
&\quad + \left((K_2K_5 - K_3K_6)\cos^3 f_0 - 3K_2K_5 \cos f_0 + (K_2K_6 + K_3K_5)\sin^3 f_0\right)\cos f \\
&\quad + \frac{3}{2\rho_0}\left(K_1K_5(e + \cos f_0) - K_1K_6 \sin f_0\right)\sin(f - f_0) \\
&\quad + \frac{3}{2}(K_2K_5 + K_3K_6) - \frac{3}{2}K_1K_5\rho J(e + \cos f) + \frac{3}{2}K_1K_6\rho J \sin f \\
&\quad + \frac{1}{2}(K_2K_5 - K_3K_6)\cos 2f - \frac{1}{2}(K_2K_6 + K_3K_5)\sin 2f
\end{aligned} \tag{24}$$

The velocity components may be computed from the derivatives of the position components but are

not relevant to the present formulation of the angles-only navigation problem. The coefficients $c_{xc}$, $c_{xs}$, and $c_{xj}$ that appear in the WLD model are defined below as functions of the observer's initial state and the integration constants of the relative motion.

$$c_{xc} = \sum_{i} \sum_{k \geq i} c_{xcik} \tag{25}$$

$$
\begin{aligned}
c_{xc11} &= \frac{3}{4} K_1^2 \frac{e + \cos f_0}{1 - e^2} \\
c_{xc12} &= \frac{3}{2} K_1 K_2 \frac{e + (1 + \rho_0 + \rho_0^2) \cos f_0}{(1 - e^2)\rho_0} \sin f_0 \\
c_{xc13} &= \frac{3}{2} K_1 K_3 \frac{-2 + e^2 + \rho_0 + (1 + \rho_0 + \rho_0^2) \cos^2 f_0}{(1 - e^2)\rho_0} \\
c_{xc14} &= \frac{3}{2} K_1 K_4 \frac{\sin f_0}{\rho_0} \\
c_{xc22} &= K_2^2 \frac{e + 6 \cos f_0 - (5 + 3\rho_0(2 + \rho_0)) \cos^3 f_0}{2(1 - e^2)} \\
c_{xc23} &= K_2 K_3 \frac{e^2 + 2(-3 + \rho_0 + \rho_0^2) + (5 + 3\rho_0(2 + \rho_0)) \cos^2 f_0}{1 - e^2} \sin f_0 \\
c_{xc24} &= K_2 K_4 \frac{4 - 3\rho_0 - (4 + 2\rho_0) \cos^2 f_0}{1 - e^2} \\
c_{xc33} &= K_3^2 \frac{-6e - 12 \cos f_0 + ((2 + e^2) + 3(1 + \rho_0)^2) \cos^3 f_0}{2(1 - e^2)} \\
c_{xc34} &= 2 K_3 K_4 \frac{2e + (2 + \rho_0) \cos f_0}{1 - e^2} \sin f_0 \\
c_{xc44} &= -\frac{3}{2} K_4^2 \frac{e + \cos f_0}{1 - e^2} \\
c_{xc55} &= -K_5^2 \frac{2(e + \cos f_0) + \cos f_0 \sin^2 f_0}{2(1 - e^2)} \\
c_{xc56} &= K_5 K_6 \frac{\sin^3 f_0}{1 - e^2} \\
c_{xc66} &= -K_6^2 \frac{e + \cos^3 f_0}{2(1 - e^2)}
\end{aligned}
$$

$$c_{xs} = \sum_i \sum_{k \geq i} c_{xsik} \tag{26}$$

$$c_{xs11} = \frac{3}{4} K_1^2 \frac{e^2 + \rho_0}{(1-e^2)\rho_0} \sin f_0$$

$$c_{xs12} = \frac{3}{4} K_1 K_2 \frac{1 + 3(\rho_0 - 1)\rho_0 - (1 + \rho_0 + \rho_0^2)\cos 2f_0}{(1-e^2)\rho_0}$$

$$c_{xs13} = \frac{3}{2} K_1 K_3 \frac{e - e\rho_0 + (1 + \rho_0 + \rho_0^2)\cos f_0}{(1-e^2)\rho_0} \sin f_0$$

$$c_{xs14} = -\frac{3}{2} K_1 K_4 \frac{e - e\rho_0 + \cos f_0}{(1-e^2)\rho_0}$$

$$c_{xs22} = -K_2^2 \frac{3 - 2\rho_0 - 3\rho_0^3 + \rho_0(5 + 3\rho_0(2 + \rho_0))\cos^2 f_0}{2(1-e^2)\rho_0} \sin f_0$$

$$c_{xs23} = K_2 K_3 \frac{e(\rho_0 - 3) - \cos f_0 (3 - \rho_0(7 + 4\rho_0(1 + \rho_0)) + \rho_0(5 + 3\rho_0(2 + \rho_0))\cos^2 f_0)}{(1-e^2)\rho_0}$$

$$c_{xs24} = -K_2 K_4 \frac{e\left(1 - \frac{3}{\rho_0}\right) + (4 + 2\rho_0)\cos f_0}{1 - e^2} \sin f_0$$

$$c_{xs33} = -K_3^2 \frac{6\rho_0(1 + \rho_0) - (3 + \rho_0)(1 - e^2) - (2(1 - e^2) + 3(1 + \rho_0)^2)\rho_0 \cos^2 f_0}{2(1-e^2)\rho_0} \sin f_0$$

$$c_{xs34} = K_3 K_4 \left( 2 \frac{4 - (2 + \rho_0)\cos^2 f_0}{1 - e^2} - \frac{3}{\rho_0} \right)$$

$$c_{xs44} = -\frac{3}{2} K_4^2 \frac{\rho_0 + e^2}{(1-e^2)\rho_0} \sin f_0$$

$$c_{xs55} = K_5^2 \left( \frac{3}{2\rho_0} - \frac{7 - \cos 2f_0}{4(1-e^2)} \right) \sin f_0$$

$$c_{xs56} = K_5 K_6 \frac{3(e + \cos f_0) - (2 + \sin^2 f_0)\rho_0 \cos f_0}{(1-e^2)\rho_0}$$

$$c_{xs66} = -K_6^2 \frac{3 - \rho_0 \sin^2 f_0}{2(1-e^2)\rho_0} \sin f_0$$

$$c_{xj} = \sum_i \sum_{k \geq i} c_{xjik} \tag{27}$$

$$c_{xj11} = K_1^2 \frac{1 - e^2 - 3\rho_0}{2(1 - e^2)}$$

$$c_{xj12} = -3K_1 K_2 \frac{\rho_0^2}{1 - e^2} \sin f_0$$

$$c_{xj13} = -K_1 K_3 \frac{3\rho_0^2}{1 - e^2} \cos f_0$$

$$c_{xj14} = 0$$

$$c_{xj22} = K_2^2 \frac{1 - 2\rho_0^3 + (\rho_0 - 1 + 3\rho_0^2(1 + \rho_0)) \cos^2 f_0}{1 - e^2}$$

$$c_{xj23} = 2K_2 K_3 \frac{e + \cos f_0 - (1 + 3\rho_0(1 + \rho_0))\rho_0 \cos f_0}{1 - e^2} \sin f_0$$

$$c_{xj24} = 2K_2 K_4 \frac{(\rho_0(1 + 2\rho_0) + e \cos f_0) \cos f_0 - e}{1 - e^2}$$

$$c_{xj33} = K_3^2 \frac{5\rho_0^2 + (e + \cos f_0)^2 - (1 - e^2 + 3\rho_0(1 + \rho_0))\rho_0 \cos^2 f_0}{1 - e^2}$$

$$c_{xj34} = -2K_3 K_4 \left( \frac{2\rho_0(1 + \rho_0)}{1 - e^2} - 1 \right) \sin f_0$$

$$c_{xj44} = K_4^2 \left( \frac{3\rho_0}{1 - e^2} - 1 \right)$$

$$c_{xj55} = K_5^2 \frac{2(1 + e^2) + (\rho_0 - 1)(5 - \cos 2f_0)}{2(1 - e^2)}$$

$$c_{xj56} = -K_5 K_6 \frac{2e \sin^3 f_0}{1 - e^2}$$

$$c_{xj66} = K_6^2 \frac{1 + (\rho_0 - 1) \cos^2 f_0}{1 - e^2}$$